

Spectral broadening caused by dynamic speckle in self-mixing velocimetry sensors

Russell Kliese and A. D. Rakić*

*The University of Queensland, School of Information Technology and Electrical Engineering,
Brisbane, QLD 4072, Australia*

[*rakic@itee.uq.edu.au](mailto:rakic@itee.uq.edu.au)

Abstract: Self-mixing laser sensors require few components and can be used to measure velocity. The self-mixing laser sensor consists of a laser emitting a beam focused onto a rough target that scatters the beam with some of the emission re-entering the laser cavity. This 'self-mixing' causes measurable interferometric modulation of the laser output power that leads to a periodic Doppler signal spectrum with a peak at a frequency proportional to the velocity of the target. Scattering of the laser emission from a rough surface also leads to a speckle effect that modulates the Doppler signal causing broadening of the signal spectrum adding uncertainty to the velocity measurement. This article analyzes the speckle effect to provide an analytic equation to predict the spectral broadening of an acquired self-mixing signal and compares the predicted broadening to experimental results. To the best of our knowledge, the model proposed in this article is the first model that has successfully predicted speckle broadening in a self-mixing velocimetry sensor in a quantitative manner. It was found that the beam spot size on the target and the target speed affect the resulting spectral broadening caused by speckle. It was also found that the broadening is only weakly dependent on target angle. The experimental broadening was consistently greater than the theoretical speckle broadening due to other effects that also contribute to the total broadening.

© 2012 Optical Society of America

OCIS codes: (280.3340) Laser Doppler velocimetry; (030.6140) Speckle; (030.6600) Statistical optics; (250.7260) Vertical cavity surface emitting lasers.

References and links

1. R. Lang and K. Kobayashi, "External optical feedback effects on semiconductor injection laser properties," *IEEE J. Quantum Electron.* **QE-16**, 347–355 (1980).
2. Y. Mitsuhashi, J. Shimada, and S. Mitsutsuka, "Voltage change across the self-coupled semiconductor laser," *IEEE J. Quantum Electron.* **QE-17**, 1216–1225 (1981).
3. J. H. Churnside, "Laser Doppler velocimetry by modulating a CO₂ laser with backscattered light," *Appl. Opt.* **23**, 61–66 (1984).
4. S. Shinohara, A. Mochizuki, H. Yoshida, and M. Sumi, "Laser Doppler velocimeter using the self-mixing effect of a semiconductor laser diode," *Appl. Opt.* **25**, 1417–1419 (1986).
5. M. Rudd, "A laser Doppler velocimeter employing the laser as a mixer-oscillator," *J. Phys. E* **1**, 723–726 (1968).
6. G. Giuliani, M. Norgia, S. Donati, and T. Bosch, "Laser diode self-mixing technique for sensing applications," *J. Opt. A Pure Appl. Opt.* **4**, 283–294 (2002).
7. L. E. Estes, L. M. Narducci, and R. A. Tuft, "Scattering of light from a rotating ground glass," *J. Opt. Soc. Am.* **61**, 1301–1306 (1971).

8. N. Takai, "Statistics of dynamic speckles produced by a moving diffuser under the Gaussian beam laser illumination," *Jpn. J. Appl. Phys.* **13**, 2025–2032 (1974).
9. E. Jakeman, "The effect of wavefront curvature on the coherence properties of laser light scattered by target centres in uniform motion," *J. Phys. A* **8**, L23–L28 (1975).
10. B. E. A. Saleh, "Speckle correlation measurement of the velocity of a small rotating rough object," *Appl. Opt.* **14**, 2344–2346 (1975).
11. P. N. Pusey, "Photon correlation study of laser speckle produced by a moving rough surface," *J. Phys. D* **9**, 1399–1409 (1976).
12. H. Jentink, F. de Mul, H. Suichies, J. Aarnoudse, and J. Greve, "Small laser Doppler velocimeter based on the self-mixing effect in a diode laser," *Appl. Opt.* **27**, 379–385 (1988).
13. Şahin Kaya Özdemir, T. Takasu, S. Shinohara, H. Yoshida, and M. Sumi, "Simultaneous measurement of velocity and length of moving surfaces by a speckle velocimeter with two self-mixing laser diodes," *Appl. Opt.* **38**, 1968–1974 (1999).
14. X. Raoul, T. Bosch, G. Plantier, and N. Servagent, "A double-laser diode onboard sensor for velocity measurements," *IEEE Trans. Instr. Meas.* **53**, 95–101 (2004).
15. R.-H. Hage, T. Bosch, G. Plantier, and A. Sourice, "Modeling and analysis of speckle effects for velocity measurements with self-mixing laser diode sensors," in *Sensors, 2008 IEEE* (IEEE, 2008), 953–956.
16. D. Han, S. Chen, and L. Ma, "Autocorrelation of self-mixing speckle in an EDFR laser and velocity measurement," *Appl. Phys. B* **103**, 695–700 (2011).
17. H. Wang, J. Shen, B. Wang, B. Yu, and Y. Xu, "Laser diode feedback interferometry in flowing Brownian motion system: a novel theory," *Appl. Phys. B* **101**, 173–183 (2010).
18. J. W. Goodman, "Statistical properties of laser speckle patterns," in *Laser Speckle and Related Phenomena*, J. C. Dainty, ed. (Springer-Verlag, 1975), chap. 2.
19. J. W. Goodman, *Statistical Optics* (John Wiley & Sons, 1985).
20. G. Giuliani and M. Norgia, "Laser diode linewidth measurement by means of self-mixing interferometry," *IEEE Photon. Technol. Lett.* **12**, 1028–1030 (2000).
21. A. Papoulis and S. U. Pillai, "Stochastic processes: General concepts," in *Probability, Random Variables, and Stochastic Processes* (McGraw Hill, 2002), chap. 9, 4th ed.
22. J. W. Goodman, "Fresnel and Fraunhofer diffraction," in *Introduction to Fourier Optics* (Roberts & Company, 2005), chap. 4, 3rd ed.
23. J. W. Goodman, "Effects of partial coherence on imaging systems," in *Statistical Optics* (John Wiley & Sons, 1985), chap. 7.
24. R. Juskaitis, N. Rea, and T. Wilson, "Semiconductor laser confocal microscopy," *Appl. Opt.* **33**, 578–584 (1994).
25. H. Albrecht, M. Borys, N. Damaschke, and C. Tropea, *Laser Doppler and Phase Doppler Measurement Techniques* (Springer Verlag, 2003).
26. R. S. Matharu, J. Perchoux, R. Kliese, Y. L. Lim, and A. D. Rakić, "Maintaining maximum signal-to-noise ratio in uncooled vertical-cavity surface-emitting laser-based self-mixing sensors," *Opt. Lett.* **36**, 3690–3692 (2011).
27. J. Scott, R. Geels, S. Corzine, and L. Coldren, "Modeling temperature effects and spatial hole burning to optimize vertical-cavity surface-emitting laser performance," *IEEE J. Quantum Electron.* **29**, 1295–1308 (1993).
28. J. W. Goodman, "Random processes," in *Statistical Optics* (John Wiley & Sons, 1985), chap. 3.
29. D. Middleton, "Spectra, covariance, and correlation functions," in *An Introduction to Statistical Communication Theory* (IEEE Press, 1996), chap. 3. Reprint.
30. D. Middleton, "Statistical preliminaries," in *An Introduction to Statistical Communication Theory* (IEEE Press, 1996), chap. 1. Reprint.
31. Y. Suzuki and A. Tachibana, "Measurement of the μm sized radius of Gaussian laser beam using the scanning knife-edge," *Appl. Opt.* **14**, 2809–2810 (1975).
32. J. M. Khosrofi and B. A. Garetz, "Measurement of a Gaussian laser beam diameter through the direct inversion of knife-edge data," *Appl. Opt.* **22**, 3406–3410 (1983).
33. R. N. Bracewell, "The basic theorems," in *The Fourier Transform and Its Applications* (McGraw Hill, 2000), chap. 6.
34. J. W. Goodman, *Introduction to Fourier Optics* (Roberts & Company, 2005), 3rd ed.
35. B. E. A. Saleh and M. C. Teich, "Beam optics," in *Fundamentals of Photonics* (Wiley, 2007), chap. 3, 2nd ed.

1. Introduction

Simple sensors can be built using semiconductor lasers when a portion of the light emitted re-enters the laser cavity causing measurable changes in the emitted power [1] and the laser terminal voltage [2]. Such 'self-mixing' sensors can be used to measure the speed of a rough moving target [3, 4]. Light scattered by a target with a velocity component parallel to the laser emission axis experiences a Doppler shift. The self-mixing sensor acts as a homodyne sys-

tem [5] whereby the Doppler shift in the reflected light leads to a periodic self-mixing signal (either acquired directly from the laser terminal voltage variations or from a photodetector that senses the variations in the optical power [4]).

Unlike a smooth surface, a rough surface makes it possible for the target to be inclined at any angle; it need not be aligned normal to the emission axis because a rough surface causes light to be scattered in all directions. An ideal self-mixing Doppler signal, in the absence of speckle effect, would be a harmonic function with a constant amplitude; in the frequency domain it would be represented by a single spectral line. However, a rough surface leads to a dynamic speckle effect causing the self-mixing Doppler signal to exhibit variations in amplitude [6] and phase. This leads to spectral broadening in the frequency domain [3].

Spectral broadening due to the dynamic speckle effect has been reported since the 1970's [7–11]. However, the literature pertaining to the effect in self-mixing sensors is more limited. The dynamic speckle effect in self-mixing sensors has been experimentally reported by several groups [12–14], and a number of models have been proposed [15, 16] including a model for the more complex problem of fluid flow with Brownian motion [17].

To the best of our knowledge, this article reports for the first time a model that has successfully predicted speckle broadening in a self-mixing velocimetry sensor in a qualitative manner that has been validated by experimental results. The model requires no parameter fitting being entirely based on the underlying optical physics of the speckle effect.

This article investigates the statistical properties of dynamic speckle from rough surfaces allowing the broadening to be predicted for given system parameters. It builds on the statistical optics foundations of Goodman [18, 19] and dynamic speckle theory published by Estes et al. [7], Jakeman [9], and Pusey [11]. The speckle model developed here applies to the self-mixing velocimetry sensor where a laser spot with Gaussian profile is focused onto the target. We show that smaller spot sizes lead to increased spectral broadening; this is particularly important for high spatial resolution sensors that make use of small laser spots. Broadening of the signal leads to uncertainty in the velocity obtained from the sensor.

Experimental verification of the speckle statistics is provided; the results are based on Vertical-Cavity Surface-Emitting Lasers (VCSELs) that are particularly well suited to self-mixing sensing applications. They typically have low threshold currents, often below one milliamper, making them suitable for mobile applications. They also often have an approximately circular, anastigmatic beam and Gaussian beam profile making optical design simpler than for edge emitting devices whose beam is elliptical and frequently astigmatic. VCSELs are also available at a low cost because of their mass production for short-haul communication links and computer mouse devices.

Apart from the speckle effect, there are several other factors that contribute to the Doppler line broadening. Firstly, a range of velocities is present over the illuminated spot region on a rotating target. This effect becomes more pronounced with the increased gradient in the velocity distribution that occurs closer to the axis of rotation. Secondly, the vibration and surface profile variation of the target adds an additional component to an otherwise constant velocity. Finally, the finite linewidth of the laser emission adds uncertainty to the fringe locations of self-mixing signals [20]. In order to concentrate this paper on speckle broadening effects alone, experimental parameters were chosen to minimize these additional sources of broadening where possible. The additional sources of broadening will be the topic of a subsequent publication.

In Sec. 2 the key results from the derivation of the Doppler signal broadening caused by the dynamic speckle effect are presented with the full derivation left to appendix A. Section 3 presents the relevant laser characteristics measured for the two lasers used in the experimental validation (with some additional details relating to the measurement of the VCSEL beam waist radius left to appendix B). Section 4 then compares the experimental results to the theory for

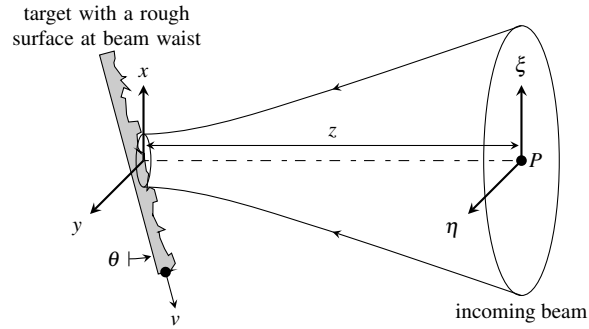


Fig. 1. Geometry used for the derivation of the dynamic speckle statistics at point P . A field which has the x, y coordinate system is incident on the rough surface moving with velocity v which is inclined at an angle θ from the x axis. This field is scattered by the rough surface and the resulting time autocorrelation function of the field at P with coordinates ξ, η is derived.

a range of target speeds, a range of spot sizes, and a range of target angles. This is followed by concluding remarks.

2. Statistical properties of speckle fields

In this section, the theory necessary to obtain the statistical properties of the light coupled back into the self-mixing sensor is presented so that an equation for the dynamic speckle broadening can be formulated. The statistical autocorrelation function for differences between observations times of the field at a point is presented (the full derivation is left to appendix A). The power spectral density of the self-mixing signal can then be obtained from the Fourier transform of the autocorrelation function [21] which can be directly compared to experimentally obtained power spectral densities of the self-mixing signal.

This analysis considers the case where the laser is focused on the target to be measured. The maximum power is coupled back into the laser under this condition, leading to the best signal-to-noise ratio (SNR); this is the configuration most used in practice. Figure 1 shows the geometry and coordinate systems used to derive the statistical autocorrelation function for the field at point P . The laser beam enters from the right and is focused onto a spot on the target which has a rough surface. The rough surface scatters the incident light producing a speckle field in the ξ - η plane. Point P is the point on the laser emission axis at a distance z from the target sufficient that the Fresnel approximations can be used to calculate the field in the ξ - η plane using the Fresnel diffraction integral. (The sufficient conditions for accuracy of the Fresnel approximation are complicated [22], but the distance z will be sufficient if P is considered to be just in front of the focusing lens discussed in Sec. 4.) Point P is the point where the coupling between the incoming field and the speckle field is obtained.

2.1. Assumptions

Several assumptions were used to simplify the problem and allow an analytic solution for the power spectral density to be obtained. These assumptions are:

1. The target is rough compared to the wavelength of illumination so that the reflected light from each point undergoes several 2π phase shifts before arriving at a phase that is uniformly distributed on the interval $(-\pi, \pi]$. This condition is satisfied by the majority of man-made and natural surfaces [23].

2. The microstructure of the scattering surface is finer than the resolving power of an aperture at point P with a diameter of the order of the beam waist diameter. This assumption of fine microstructure allows the spatial autocorrelation function of the target to be well approximated by a delta function [18].
3. The spatial extent of the spot is sufficient so that a large number of individual scattering sites are illuminated.
4. The laser emission is monochromatic.
5. Only one polarization is considered and depolarization effects are ignored. This assumption makes the derivation of the model tractable.
6. The speckle grain size is sufficiently large so that the field variation over the illuminated region at P is insignificant (the speckle grain will have a linear dimension of the order of $\lambda z/r$ where λ is the laser emission wavelength and r is the spot radius [7]).
7. The wave-fronts of the incoming beam and the scattered beam at P have identical curvature. The spherical scattered field will approximate the incoming field on the axis when focused to a small spot on the target.
8. The change in intensity at point P is proportional to the change in the laser terminal voltage. This is valid for the weak feedback regime used in the experiments. The equivalence between the intensity and the laser terminal voltage variation has been demonstrated experimentally [4] and is supported by a theoretical model [24].

2.2. Statistical time-autocorrelation function

In this section we present the autocorrelation function for the field at P . The field at P will have a Gaussian probability distribution by the central limit theorem because it is the sum of many independent random variables: the components from many different scatterers on the rough surface. Therefore, the autocorrelation function and mean completely describe the random process. Furthermore, the mean is zero (see Appendix A).

The statistical autocorrelation function of the field amplitude R_A , at P as a function of the difference between observation times τ , is:

$$R_A(\tau) = \frac{\exp\left(i\frac{4\pi v\tau \sin \theta}{\lambda}\right)}{\lambda^2 z^2} \iint_{-\infty}^{\infty} U(x + v\tau \cos \theta, y) U^*(x, y) \times \exp\left\{\frac{i\pi \left[(x + v\tau \cos \theta)^2 - x^2\right]}{\lambda z}\right\} dx dy. \quad (1)$$

where λ is the wavelength of the laser emission, θ is the inclination angle of the target, U is the field incident on the rough surface, $*$ denotes the complex conjugate, and i is the imaginary unit ($\sqrt{-1}$).

Surface profile parameters are absent from Eq. (1) due to assumption 1 in Sec. 2.1. This Independence of broadening on surface microstructure has been validated experimentally by measuring the broadening from a sand-blasted aluminum surface and from a paper surface. Under a range of conditions, the broadenings obtained from both surfaces were identical.

VCSELs used for self-mixing sensors often have emission profiles that are approximately Gaussian. An analytic result can be obtained for the autocorrelation function for the specific

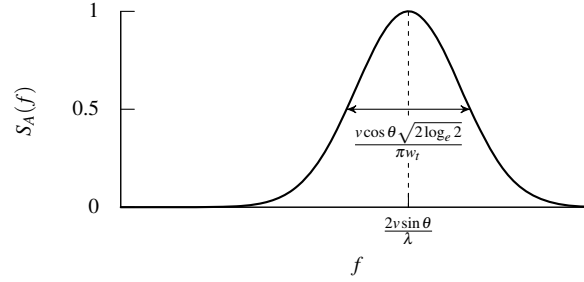


Fig. 2. A plot of the normalised power spectral density with the FWHM and peak frequency indicated.

case of Gaussian illumination specified by the beam waist radius at the target w_t . If the Gaussian field,

$$U_G(x, y) = \frac{2}{\pi w_t^2} \exp\left(-\frac{x^2 + y^2}{w_t^2}\right), \quad (2)$$

is substituted into Eq. (1), the normalised power spectral density can be obtained as a function of frequency f ,

$$S_A(f) = \exp\left[-\frac{2\pi^2 w_t^2 (f - \frac{2v \sin \theta}{\lambda})^2}{v^2}\right]. \quad (3)$$

This result makes use of an approximation valid for small spot sizes (see Sec. 6.1 in appendix A for details). In this work, the spectral broadening is quantified by measuring the full-width half-maximum (FWHM) of the Doppler signals. The FWHM of Eq. (3) is:

$$\text{FWHM} = \frac{v \cos \theta \sqrt{2 \log_e 2}}{\pi w_t}. \quad (4)$$

The peak frequency f_D , is the parameter used to obtain the target velocity in self-mixing velocimetry sensors and is given by:

$$f_D = \frac{2v \sin \theta}{\lambda}, \quad (5)$$

which is in agreement with the Doppler frequency from [25].

A plot of $S_A(f)$, with the FWHM and peak labeled, appears in Fig. 2. The simple analytic formula for the FWHM can be used to predict spectral broadening for self-mixing sensors. This result shows that the speckle broadening of Doppler self-mixing signal depends only on the component of the target velocity normal to the optical axis and the beam waist radius on the target. Notably it does not depend explicitly on wavelength, and is independent of the target inclination angle in the small angle approximation.

3. Laser characterization

In order to validate the dynamic speckle theory, we wanted to choose representative lasers used for self-mixing interferometry. In order to simplify the analysis, we limited the choice of lasers to VCSELs operating in a single transverse mode, which is typically obtained from devices with small apertures. We chose two mass produced VCSELs, one with visible emission (Firecomms, RVM665T) and one with infra-red emission (Littrax, LX-VCS-850-T311), with nominal emission wavelengths of 665 nm and 850 nm respectively. All measurements were made at room temperature of approximately 25°C.

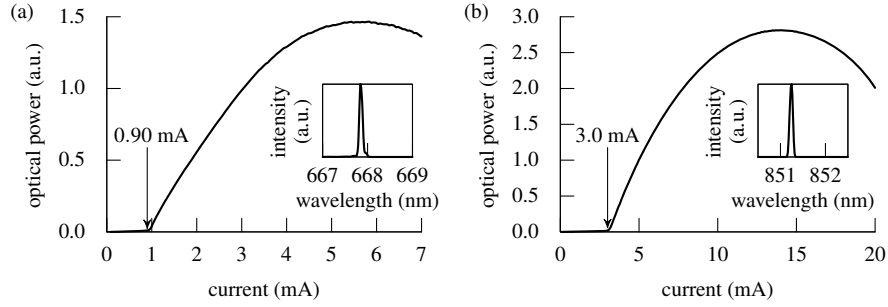


Fig. 3. Light-current plots for the Firecomms laser (a) and the Litrax laser (b) used in the experiments showing threshold currents measured at 25°C. The power rollover is typical of VCSELs [27]. The insets show the emission spectra for the Firecomms and Litrax lasers at 1.00 mA and 4.08 mA respectively; both lase with a single mode.

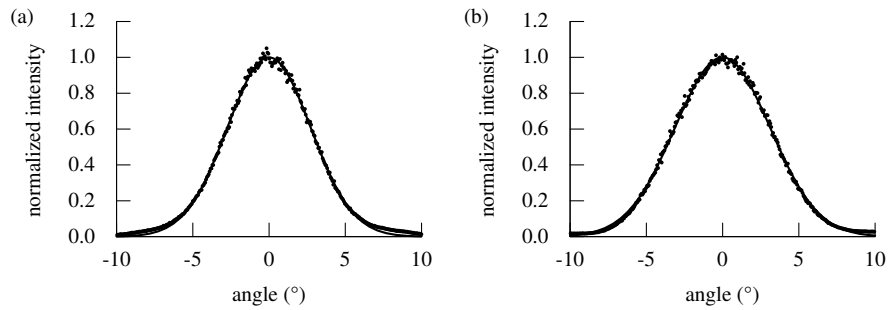


Fig. 4. Plots of the laser far-field profiles obtained from the CCD (circles) and the Gaussian fits (solid lines) used to infer the laser beam waist radii for the Firecomms laser (a) with an extracted beam waist diameter of 2.22 μm and the Litrax laser (b) with an extracted beam waist diameter of 2.48 μm .

3.1. Light-current

Light-current plots for the lasers were measured in order to identify the threshold currents (see Fig. 3). The laser bias currents were chosen to be close to threshold where self-mixing sensors usually yield the highest SNR [26] and higher order modes are likely to be weakest. The Firecomms laser was operated at 1.00 mA and the Litrax laser at 4.08 mA.

3.2. Laser spot size

To estimate the spot size on the target w_t , we measured the VCSEL waist radius w_0 , and multiplied by the magnification of the optical system α :

$$w_t = \alpha w_0. \quad (6)$$

The VCSEL waist radius w_0 , was inferred from the beam in the far-field. The beam profile was acquired using a high dynamic-range camera. The beam profile was fitted to the Gaussian function in order to extract the beam parameters as shown in Fig. 4. From these measurements w_0 for both lasers was calculated (Table 1). Additional details of the beam profiling process are included in appendix B.

Table 1. Parameters of the two lasers used for experimental validation of the dynamic speckle theory.

manufacturer	Firecomms	Litrax
model number	RVM665T	LX-VCS-850-T311
bias current	1.00 mA	4.08 mA
wavelength	668 nm	851 nm
beam waist radius	2.22 μm	2.48 μm

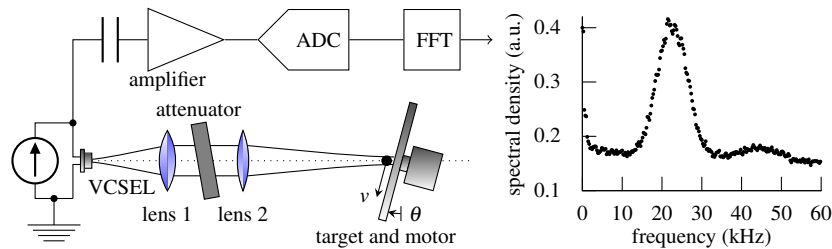


Fig. 5. Schematic of the experimental setup used to obtain Doppler velocimetry signals along with a typical averaged spectrum. The setup is shown looking from above with the laser beam waist imaged onto the disc below the axis of rotation such that there is a component of velocity in the direction of the optical axis. The attenuator is used to keep the sensor operating in the weak feedback regime. The laser is driven by a constant current source. The laser terminal voltage variations are amplified, then sampled to produce a spectrum via the FFT.

4. Experimental results

The broadening for a range of target velocities, target inclination angles, and spot-sizes were measured. This was accomplished using the setup shown schematically in Fig. 5. The two lenses, with focal lengths f_1 and f_2 , were chosen from a range of microscope lenses in order to produce a range of different sized laser spot images on the target (see Table 2). The beam is attenuated to keep the sensor operating in the weak feedback regime. The target consisted of paper on the face of an aluminum disc attached to a dc motor. The motor's speed was controlled using feedback from an optical encoder and a digital motor controller. The small voltage variations induced by light scattered from the target were amplified and then digitized using an analog-to-digital converter (ADC). The digitized signal was then transformed into the frequency domain using a fast Fourier transform (FFT). One hundred FFTs were averaged to provide a close approximation to the ensemble average. The FWHM broadening was obtained by fitting the sum of a Gaussian function and a constant term (to account for noise) to the resulting spectra over a frequency region around the peak. The free parameters of the fit were the Gaussian FWHM (the parameter of interest), the Gaussian amplitude, the Gaussian center frequency and the constant.

Several methods were used to ensure that the broadening due to the Dynamic speckle effect would dominate the other sources of broadening. Because the speckle broadening is inversely proportional to the spot size, small spot sizes were chosen. To reduce the effect of the velocity variation over the spot region on the disc, the spot was formed at a large distance from the center of the disc relative to the spot size. Tight control of the disc velocity was provided by a digital motor controller. A rigid motor mounting bracket was used to limit vibration.

All FWHM broadening measurements were repeated several times and measurement uncertainty was much smaller than the additional broadening observed above the theoretical broad-

Table 2. The focal lengths and resulting magnifications for lens combinations used to obtain a range of spot sizes on the target.

f_1 (mm)	f_2 (mm)	magnification
16	26.7	1.67
8	16	2.00
16	40	2.50
8	26.7	3.33
8	40	5.00

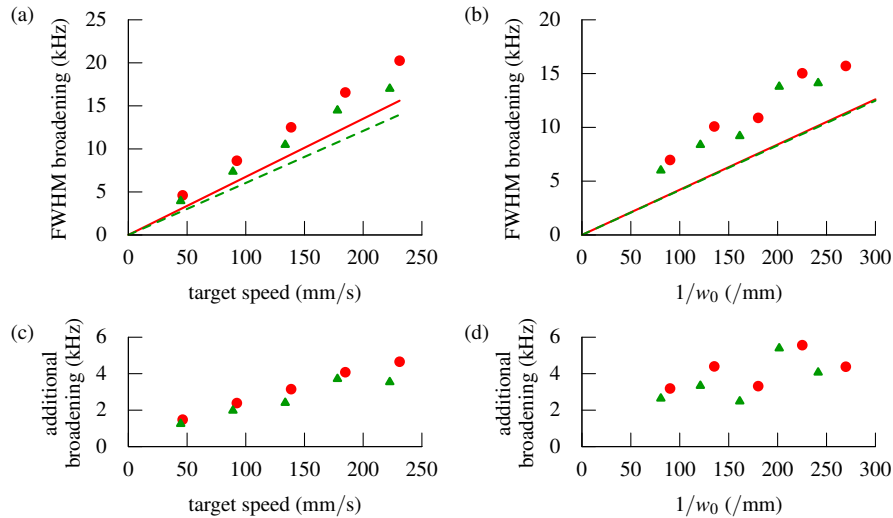


Fig. 6. Doppler peak broadening for a range of target speeds measured using a $2.5\times$ imaging lens configuration (a), and for a range of spot sizes on the target with a fixed target velocity of 111 mm/s (b). The circles and triangles show the experimental broadening measurements acquired from the Firecomms and Litrax lasers respectively. The solid and broken lines indicate the theoretical broadening for the Firecomms and Litrax lasers respectively. Plots (c) and (d) show the differences between the experimental broadening (which includes all broadening effects) and the theoretical values that only include speckle broadening.

ening due to speckle.

4.1. Effect of target speed on broadening

According to Eq. (4), the broadening is proportional to the target velocity. The target velocity was varied by changing the disc rotational speed using the motor controller. The target velocity was calculated from the radial distance measured from the center of the disc to the spot location. The inclination angle was fixed at 10° . Figure 6(a) shows the experimental results and the theoretical broadening based on the beam waist radii in Table 1 and the $2.5\times$ magnification factor of the imaging system.

The experimental broadening is consistently greater than the theoretical speckle broadening as can be expected due to a range of other factors that contribute to the broadening of the Doppler signal. However, the proportionality of the broadening to the target speed agrees with the theory. The additional broadening of the measured values is also proportional to the disc speed as can be seen in Fig. 6(c).

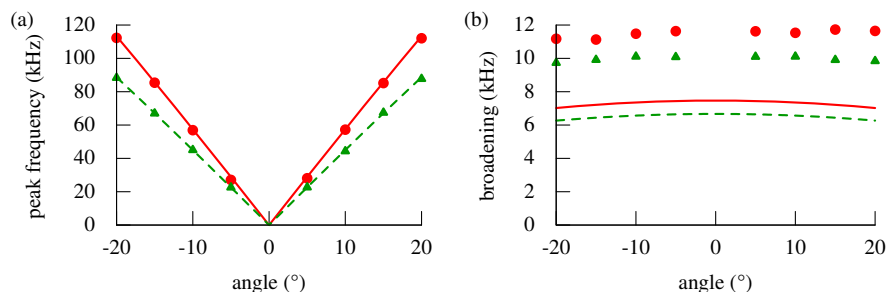


Fig. 7. Doppler peak frequency (a) and FWHM broadening (b) with a fixed target speed of 111 mm/s over a range of target angles. The circles and triangles show the experimental broadening measurements acquired from the Firecomms and Littrax lasers respectively. The solid and broken lines indicate the theoretical broadening for the Firecomms and Littrax laser's respectively.

4.2. Effect of spot size on broadening

A range of spot sizes were generated using combinations of microscope lenses. The laser spot was magnified according to the values listed in Table 2. Figure 6(b) show the measured results along with the theoretical broadening. Again, the experimental broadening is consistently larger than the theoretical broadening. However, in contrast to the additional broadening in Fig. 6(c), the additional broadening in Fig. 6(d) is not strongly correlated to the inverse of the spot size. The slope of the experimental results show a good match to the theory. These results also confirm the independence of broadening on laser wavelength as expected by the theory — the two lasers have substantially different wavelengths yet the broadening only depends on the spot size.

The results in Fig. 6(a) and (b) show two slices through a two-dimensional continuum of possible results depending on the spot size and target speed. Based on the results obtained, the additional spectral broadening over this continuum scales with the target speed, but is relatively independent of the laser spot size. The additional broadening may therefore be predominantly due to an effect that scales with the target speed such as target vibration.

4.3. Effect of target angle on broadening

One perhaps unexpected result from the theoretical investigation was the cosine dependence of the Doppler signal broadening with target inclination angle. This is in contrast to the peak frequency f_D , in Eq. (5) which has a sine dependence on the target inclination angle.

Figure 7(a) shows the experimentally obtained Doppler peak frequency and the theoretical values in close agreement. Figure 7(b) shows the Doppler broadening results that are largely independent of the target angle. Again, the experimentally obtained broadening results are greater than the theory predicts.

5. Conclusions

The speckle theory derived in this paper gives a simple analytic model that can be used to predict spectral broadening for self-mixing sensors. The model provides insight in the dependence of Doppler spectrum characteristics as a function of spot size on the target and the target velocity. It also shows the interesting independence of the Doppler signal broadening on the angle of incidence for target inclination angles close to normal. This is in contrast to the strong dependence of the Doppler peak frequency on angle. Comparison between the model and the experimental results was presented for two typical mass-produced VCSELs. The measured

broadening was consistently larger than the theory predicts due to other effects that contribute to broadening. Other contributing effects include the range of velocities present over the illuminated region on a rotating target, vibration, surface profile variation and the laser linewidth. The experimental results suggest that vibration is the dominant source of the additional broadening. However, these contributing mechanisms leading to additional broadening are not of fundamental nature, and could be removed by the experimental design.

6. Appendix A: Derivation of the field amplitude autocorrelation function and power spectrum

In this section we derive the autocorrelation function for the dynamic speckle process for a general field distribution. We then solve for the specific case of a Gaussian field and apply a simplification valid for small waist radii to obtain the simple analytic result used in the preceding sections of the paper.

The dynamic speckle process is ergodic allowing the time autocorrelation and statistical autocorrelation functions to be interchanged [28] or [29]. Both forms are used here as convenient.

Referring to the geometry in Fig. 1, the statistical autocorrelation function of the field amplitude R_A , at P as a function of times t_1 and t_2 is [28]

$$R_A(t_1, t_2) = \mathbf{E}[A(t_1)A^*(t_2)], \quad (7)$$

where $\mathbf{E}[\cdot]$ denotes the expected value operator [30] and $A(t)$ is the complex field amplitude at P .

Because $A(t)$ is a stationary process (a necessary condition for ergodicity), the time difference $\tau = t_2 - t_1$, only need to be considered. Therefore Eq. (7) can be rewritten as

$$R_A(\tau) = \mathbf{E}[A(t - \tau)A^*(t)]. \quad (8)$$

If the surface is rough compared to the wavelength, the field at each point, (x, y) , reflected from the rough surface of the target is given a phase shift ϕ , that is uniformly distributed over $(-\pi, \pi]$. We define $\Psi(x, y) = e^{i\Phi(x, y)}$ where $\Phi(x, y)$ is a random variable for phase shift due to the rough surface. If the target is inclined at an angle θ , from the perpendicular orientation, the complex field reflected from the target will undergo an additional phase shift,

$$V(x, y) = \exp\left(i\frac{4\pi x \tan \theta}{\lambda}\right). \quad (9)$$

The complex field reflected and just to the right of the target $\alpha(x, y)$, is given by the product of the incident field $U(x, y)$, the phase shift due to the inclination of the target, and the random phase shift:

$$\alpha(x, y) = U(x, y)V(x, y)\Psi(x, y), \quad (10)$$

with $\Psi(x, y)$ being a random variable.

The Huygens-Fresnel principle can be used to relate the field at the target plane $\alpha(x, y)$, to the field at the observation point $A(\xi, \eta)$. This is approximated by the Fresnel diffraction integral [22],

$$A(\xi, \eta) = \frac{\exp(i\frac{2\pi z}{\lambda})}{i\lambda z} \exp\left[\frac{i\pi}{\lambda z}(\xi^2 + \eta^2)\right] \times \iint_{-\infty}^{\infty} \alpha(x, y) \exp\left[\frac{i\pi}{\lambda z}(x^2 + y^2)\right] \exp\left[\frac{i\pi}{\lambda z}(\xi x + \eta y)\right] dx dy. \quad (11)$$

The integral is simplified because only a single point is considered in the observation plane and constant phase terms can be removed without affecting the statistical properties of the phase because it is uniformly distributed over $(-\pi, \pi]$. Therefore

$$A(t) = \frac{1}{\lambda z} \iint_{-\infty}^{\infty} \alpha(x, y, t) \exp \left[\frac{i\pi}{\lambda z} (x^2 + y^2) \right] dx dy. \quad (12)$$

We now consider the target in Fig. 1 moving with velocity v . For a fixed laser, the illumination field amplitude $U(x, y)$, and the reflected field amplitude are identical and do not change with time. On the other hand, the random phase variations due to the rough surface Ψ , will be shifted in the x direction a distance $vt \cos \theta$. Therefore, the reflected field just to the right of the rough target in Fig. 1 is

$$\alpha(x, y, t) = \Psi(x + vt \cos \theta, y) U(x, y) V(x, y). \quad (13)$$

It is now possible to calculate the autocorrelation function of the field at P , $R_A(t_1, t_2)$, from Eq. (7) using the simplified Fresnel diffraction integral in Eq. (12) and the reflected field given in Eq. (13).

$$R_A(t_1, t_2) = \mathbf{E} \left[\frac{1}{\lambda z} \iint_{-\infty}^{\infty} \Psi(x + vt_1 \cos \theta, y) U(x, y) V(x, y) \exp \left[\frac{i\pi (x^2 + y^2)}{\lambda z} \right] dx dy \right. \\ \left. \times \text{conj} \left\{ \frac{1}{\lambda z} \iint_{-\infty}^{\infty} \Psi(x + vt_2 \cos \theta, y) U(x, y) V(x, y) \exp \left[\frac{i\pi (x^2 + y^2)}{\lambda z} \right] dx dy \right\} \right] \quad (14)$$

Where x has been substituted with $x + vt \cos \theta$ to represent motion in the x direction. It is possible to consider motion in any direction by altering the orientation of the axes so that the x -axis lies in the direction of motion. Therefore, only considering motion in the x direction does not limit the generality of the result.

If the order of integration is changed, the following form is obtained

$$R_A(t_1, t_2) = \frac{1}{\lambda^2 z^2} \iiint_{-\infty}^{\infty} \mathbf{E} [\Psi(x_1 + vt_1 \cos \theta, y_1) \Psi^*(x_2 + vt_2 \cos \theta, y_2)] \\ \times U(x_1, y_1) V(x_1, y_1) U^*(x_2, y_2) V^*(x_2, y_2) \exp \left[\frac{i\pi (x_1^2 + y_1^2 - x_2^2 - y_2^2)}{\lambda z} \right] dx_1 dy_1 dx_2 dy_2. \quad (15)$$

While Eq. (15) looks complicated, it is dramatically simplified under the assumption of very fine microstructure of the scattering surface. The spatial autocorrelation of the random phase screen becomes a delta function [18],

$$\mathbf{E} [\Psi(x_1 + vt_1 \cos \theta, y_1) \Psi^*(x_2 + vt_2 \cos \theta, y_2)] = \delta(x_2 + vt_2 \cos \theta - x_1 - vt_1 \cos \theta, y_2 - y_1), \quad (16)$$

which is non-zero only when its parameters are zero. Replacing $t_2 - t_1$ with τ , Eq. (16) becomes

$$\delta(x_2 - x_1 + v\tau \cos \theta, y_2 - y_1). \quad (17)$$

Upon substituting this into Eq. (15), and considering the integration with respect to dx_1 and dy_1 , the delta-function is non-zero when $x_1 = x_2 + v\tau \cos \theta$ and $y_1 = y_2$, therefore we can rewrite Eq. (15) as

$$R_A(\tau) = \frac{1}{\lambda^2 z^2} \iint_{-\infty}^{\infty} U(x_2 + v\tau \cos \theta, y_2) V(x_2 + v\tau \cos \theta, y_1) U^*(x_2, y_2) V^*(x_2, y_2) \\ \exp \left\{ \frac{i\pi [(x_2 + v\tau \cos \theta)^2 - x_2^2]}{\lambda z} \right\} dx_2 dy_2. \quad (18)$$

The phase terms due to the inclination of the target can be expanded:

$$\begin{aligned}
 V(x_2 + v\tau \cos \theta, y_1) V^*(x_2, y_2) &= \exp \left[i \frac{4\pi(x_2 + v\tau \cos \theta) \tan \theta}{\lambda} \right] \exp \left[-i \frac{4\pi x_2 \tan \theta}{\lambda} \right] \\
 &= \exp \left(i \frac{4\pi v\tau \cos \theta \tan \theta}{\lambda} \right) \\
 &= \exp \left(i \frac{4\pi v\tau \sin \theta}{\lambda} \right). \tag{19}
 \end{aligned}$$

This term, which is related to the Doppler frequency as described subsequently, is independent of x_2 and y_2 , so can be moved outside of the integral in Eq. (18) yielding

$$R_A(\tau) = \frac{\exp \left(i \frac{4\pi v\tau \sin \theta}{\lambda} \right)}{\lambda^2 z^2} \iint_{-\infty}^{\infty} U(x_2 + v\tau \cos \theta, y_2) U^*(x_2, y_2) \exp \left\{ \frac{i\pi \left[(x_2 + v\tau \cos \theta)^2 - x_2^2 \right]}{\lambda z} \right\} dx_2 dy_2. \tag{20}$$

This is reproduced in Eq. (1) in Sec. 2 with x_2 replaced by x and y_2 replaced by y .

6.1. Gaussian field

We now solve the statistical autocorrelation function for the specific case of a Gaussian field. We substitute Eq. (2) into Eq. (1) and solve the integral as follows:

$$\begin{aligned}
 R_A(\tau) &= \frac{\exp \left(i \frac{4\pi v\tau \sin \theta}{\lambda} \right)}{(\lambda z)^2} \iint_{-\infty}^{\infty} \frac{4}{(\pi w_t^2)^2} \exp \left[-\frac{(x + v\tau \cos \theta)^2 + y^2 + x^2 + y^2}{w_t^2} \right] \\
 &\quad \times \exp \left\{ \frac{i\pi \left[(x + v\tau \cos \theta)^2 - x^2 \right]}{\lambda z} \right\} dx dy \\
 &= \frac{4 \exp \left(i \frac{4\pi v\tau \sin \theta}{\lambda} \right)}{(\lambda z \pi w_t^2)^2} \int_{-\infty}^{\infty} \exp \left(-\frac{2y^2}{w_t^2} \right) \\
 &\quad \times \int_{-\infty}^{\infty} \exp \left\{ \frac{i\pi}{\lambda z} \left[(x + v\tau)^2 - x^2 \right] - \frac{1}{w_t^2} \left[(x + v\tau)^2 + x^2 \right] \right\} dx dy \\
 &= \frac{4 \exp \left(i \frac{4\pi v\tau \sin \theta}{\lambda} \right)}{(\lambda z \pi w_t^2)^2} \int_{-\infty}^{\infty} \exp \left(-\frac{2y^2}{w_t^2} \right) \frac{\sqrt{\pi} w_t}{\sqrt{2}} \exp \left[-\frac{v^2 \tau^2}{2} \left(\frac{\pi^2 w_t^2}{\lambda^2 z^2} + \frac{1}{w_t^2} \right) \right] dy \\
 &= \frac{4}{(\lambda z \pi w_t^2)^2} \sqrt{\pi} w_t \frac{\sqrt{\pi} w_t}{\sqrt{2}} \exp \left[-\frac{v^2 \tau^2}{2} \left(\frac{\pi^2 w_t^2}{\lambda^2 z^2} + \frac{1}{w_t^2} \right) + i \frac{4\pi v\tau \sin \theta}{\lambda} \right] \\
 &= \frac{2\sqrt{2}}{\pi (\lambda z w_t)^2} \exp \left[-\frac{v^2 \tau^2}{2} \left(\frac{\pi^2 w_t^2}{\lambda^2 z^2} + \frac{1}{w_t^2} \right) + i \frac{4\pi v\tau \sin \theta}{\lambda} \right]. \tag{21}
 \end{aligned}$$

This result, ignoring the Doppler term, $i \frac{4\pi v\tau \sin \theta}{\lambda}$, is in agreement with [9, 11] for the case when the beam waist is located on the target and the distance between the detectors is zero.

$A(t)$ will have a Gaussian probability distribution by the central limit theorem because it is the sum of many independent random variables. Therefore, the autocorrelation function and mean completely describe the random process. Furthermore, the mean $m = \mathbf{E}[A(t)]$, is zero because $\mathbf{E}[\Psi(t)] = 0$.

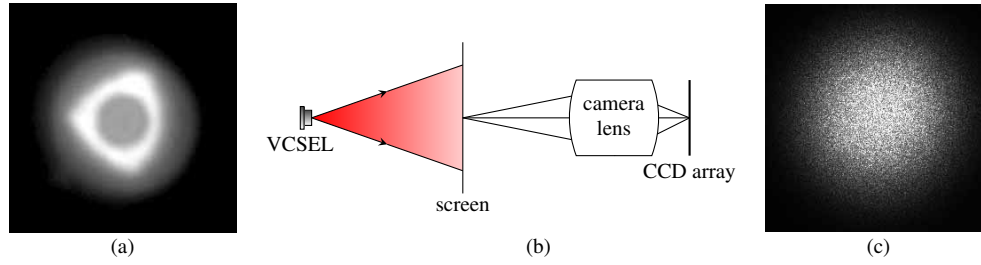


Fig. 8. (a) Near-field image of Firecomms laser below threshold (0.21 mA) suggestive of non-circular carrier injection. The disc where emission is present is defined by the metalization on the front facet of the laser. Non-uniform proton implantation may be responsible for the irregular emission shape. (b) Diagram of the setup used to infer the laser near-field spot size from a far-field image. (c) A sample far-field image obtained from the CCD array. The speckle caused by the rough surface of the screen is evident in the CCD image.

6.1.1. Simplification for a small Gaussian spot

If w_t is small, the $\pi^2 w_t^2 / \lambda^2 z^2$ term in Eq. (21) becomes insignificant compared to $1/w_t^2$, or

$$\frac{\pi^2 w_t^4}{\lambda^2 z^2} \ll 1. \quad (22)$$

For example, using the experimental conditions for the Litrax laser with the greatest waist radius on the target (12.4 μm), Eq. (22) yields ≈ 0.0002 . Making use of this simplification and normalizing, Eq. (21) becomes:

$$R_A(\tau) = \exp \left(-\frac{v^2 \tau^2}{2w_t^2} + i \frac{4\pi v \tau \sin \theta}{\lambda} \right). \quad (23)$$

The normalised spectrum is therefore:

$$S_A(f) = \mathcal{F}\{R_A(\tau)\} / \max(\mathcal{F}\{R_A(\tau)\}) = \exp \left[-\frac{2\pi^2 w_t^2 \left(f - \frac{2v \sin \theta}{\lambda} \right)^2}{v^2} \right]. \quad (24)$$

This result is reproduced in Eq. (3) in Sec. 2.2 and plotted in Fig. 2.

7. Appendix B: Experimental procedure used to measure the beam waist radius

For a perfect Gaussian beam it is possible to use a knife-edge technique to measure the focused spot size directly [31, 32]. However, in this work, the VCSEL near-fields departed from a circular profile. The image of the Firecomms laser near-field taken below threshold in Figure 8(a) is suggestive of non-uniform carrier injection leading to the non-circular near-field profile.

In contrast to the laser near-field profiles, the laser far-field profiles were more circular and provided good fits to the ideal Gaussian beam profile. Additionally, the relationship between the laser far-field profile and the self-mixing signal power spectrum is more direct. This can be seen by considering that the self-mixing signal power spectrum in Eq. (24) is obtained from the Fourier transform of the autocorrelation function in Eq. (1). In the small spot approximation (such that the phase terms in the integral are small), Eq. (1) is simply the autocorrelation of the field on the target. Recalling the autocorrelation theorem [33],

$$\int_{-\infty}^{\infty} f(u) f^*(u+x) du = |\mathcal{F}\{f\}|^2, \quad (25)$$

the self-mixing signal power spectrum is therefore related to the spatial power spectrum (spatial power distribution) of the field on the target. In a similar way, and fundamental to the field of Fourier optics [34], the laser far-field intensity (as measured by the CCD array) is also the spatial power spectrum of the laser near-field which is a reduced version of the field on the target. Therefore, the laser far-field intensity distribution and the self-mixing power spectrum are closely related.

For these reasons, the laser far-field images were used to infer the laser beam waist radii.

Figure 8(b) shows how a CCD array was used to capture an image of the laser far-field profile that was projected onto a screen [a sample image appears in Fig. 8(c)]. A camera lens was used to reduce the profile image to fit on the CCD array. The resulting two-dimensional matrix of intensities from the CCD was reduced to a one-dimensional vector by integrating each vertical column. The vectors obtained for each of the two VCSELs were plotted in Fig. 4. In order to obtain the VCSEL waist radius, the one-dimensional data was fitted to a Gaussian function that we now derive. A Gaussian beam [35] has the following intensity profile:

$$I(x, y) \propto \exp \left[-\frac{2(x^2 + y^2)}{w^2(z)} \right], \quad (26)$$

where z is the distance from the beam waist, z_R (the Rayleigh parameter) is equal to $\pi w_0^2/\lambda$, and

$$w(z) = w_0 \sqrt{1 + \left(\frac{z}{z_R} \right)^2}. \quad (27)$$

The integration of the CCD array columns corresponds to integration over y giving:

$$I(x) \propto \exp \left[-\frac{2x^2}{w^2(z)} \right]. \quad (28)$$

In the far-field, $z \gg z_R$, therefore, $w(z) \approx z\lambda/(\pi w_0)$. The laser wavelengths λ , were measured for each laser using an optical spectrum analyzer (Agilent 86140B, resolution 0.07 nm, accuracy ± 0.5 nm) for the bias conditions used in the experiments; they are recorded in Table 1. Substituting $w(z)$ with the far-field approximation into Eq. (28) and making use of the small angle approximation, $r/z \approx \theta$, we obtain:

$$I(\theta) \propto \exp \left[-2 \left(\frac{\pi \theta w_0}{\lambda} \right)^2 \right]. \quad (29)$$

This function was fitted to the data obtained from the CCD images in Fig. 4 in order to extract the beam-waist radii which appear in Table 1.

Acknowledgements

Russell Kliese is grateful to Thomas Taimre for his valuable feedback while undertaking the work that led to this article. This research was supported under Australian Research Councils Discovery Projects funding scheme (DP0988072).